GEOPHYSICS

Mechanism of large-scale flow reversals in turbulent thermal convection

Yin Wang[1], Pik-Yin Lai[2], Hao Song[1,3], Penger Tong[1]*

It is commonly believed that heat flux passing through a closed thermal convection system is balanced so that the convection system can remain at a steady state. Here, we report a new kind of convective instability for turbulent thermal convection, in which the convective flow stays over a long steady "quiet period" having a minute amount of heat accumulation in the convection cell, followed by a short and intermittent "active period" with a massive eruption of thermal plumes to release the accumulated heat. The rare massive eruption of thermal plumes disrupts the existing large-scale circulation across the cell and resets its rotational direction. A careful analysis reveals that the distribution of the plume eruption amplitude follows the generalized extreme value statistics with an upper bound, which changes with the fluid properties of the convecting medium. The experimental findings have important implications to many closed convection systems of geophysical scale, in which massive eruptions and sudden changes in large-scale flow pattern are often observed.

INTRODUCTION

Massive eruption events and sudden changes in large-scale flow pattern are often observed in closed thermal convection systems of geophysical scale, such as in oceanic circulation, Earth's outer core convection, and dynamo generation of geomagnetic field, and in the convective zone of the sun and other stars and planets (*1*–*6*). While the incidence of these events is rare, their impact to our living conditions is often dramatic. Because of the complexity of the phenomena owing to the extreme conditions and complex material parameters involved (*7*), our fundamental understanding of the geophysical-scale flow phenomena is often challenged by limited direct experimental observations and oversimplified computer simulations.

In the laboratory, controlled turbulent convection can be realized and systematically studied in a closed Rayleigh-Bénard cell, which is heated from below and cooled from the top with a vertical temperature gradient parallel to gravity. When the temperature difference ΔT across the fluid layer or the associated dimensionless buoyancy, the Rayleigh number Ra, is sufficiently large ($Ra \gtrsim 10^8$), the bulk fluid becomes turbulent and a large-scale circulation (LSC) is formed across the height of the convection cell (*8*, *9*). The LSC is driven by the warm and cold plumes emitted from the unstable thermal boundary layers near the top and bottom conducting plates and is maintained at a steady state in a turbulent environment (*10*–*13*). This large-scale flow has been studied extensively in the upright cylindrical cells of aspect ratio unity, in which the LSC has a single roll structure, with its size comparable to the cell height.

An intriguing feature of the LSC is its irregular cessation, a momentary vanishing of the entire circulation flow followed by a restart of LSC in a randomly chosen new direction (*14*–*17*). If the new LSC rotates in the same direction as that of the original LSC, it is called a cessation event; otherwise, it is called a reversal event. While a number of theoretical models based on either stochastic or deterministic differential equations (*18*–*26*) have been proposed to explain the experimental findings, a unified understanding of the phenomenon has not been achieved. Up to now, most of the convection experiments aimed at testing the theoretical models were conducted in either cylindrical or rectangular cells, in which the LSC does not fit the cell geometry well and its dynamics is complicated by secondary (corner) flows in the cell. As a result, a general mechanism for the LSC cessations and reversals still remains elusive.

Here, we report a novel convection experiment conducted in a specially designed thin disc cell, with its circular plane orientated vertically parallel to gravity. Because the cell shape matches the single-roll structure of the LSC perfectly, there is not any corner flow inside the cell. This is a "simple but not simpler" convection system, which has key features of turbulent convection (*27*) and offers a natural way to study the fundamental instabilities of the LSC. The thin disc cell also allows us to conduct a precise shadowgraph measurement to detect the net accumulation or loss of heat flux across the entire cell and to visualize the LSC and plume dynamics. A central finding of this investigation is that the convective flow is in a dynamically chaotic state, with a long steady "quiet period" having a minute amount of heat accumulation in the convection cell, followed by a short and intermittent "active period" with a massive eruption of thermal plumes to release the accumulated heat. The rare massive eruption of thermal plumes disrupts the LSC so that its rotation is reset after each eruption event with an equal probability to be in either clockwise or anticlockwise directions.

RESULTS

The vertical thin disc used in the convection experiment has a diameter $D = 188$ mm and a thickness $W = 20$ mm so that the aspect ratio $\Gamma \equiv W/D = 0.11$. There are two control parameters in the experiment: one is the Rayleigh number Ra, which is varied in the range $3 \times 10^9 \lesssim Ra \lesssim 2 \times 10^{10}$, and the other is the Prandtl number Pr, which is fixed for a given fluid. Three working fluids are used: one is distilled water ($Pr = 4.4$) and the other two are 10 weight % (wt %) ($Pr = 5.7$) and 20 wt % ($Pr = 7.6$) aqueous solutions of glycerin.

In the experiment, we use the shadowgraph technique to visualize the LSC and thermal plumes. When a parallel beam of light passes through a convecting fluid, its transmission intensity $I(x, y, t)$ (or shadowgraph), as shown in Fig. 1 (A and B), is related to the second-order spatial derivative (Laplacian) of the refractive index variation $n(x, y, t)$ due to temperature fluctuations $T(x, y, t)$ in the convective flow. For

[1]Department of Physics, Hong Kong University of Science and Technology, Clear Water Bay, Kowloon, Hong Kong. [2]Department of Physics and Center for Complex Systems, National Central University, Chungli, Taiwan 320, R.O.C. [3]College of Physics and Energy, Shenzhen University, Shenzhen 518060, P. R. China.
*Corresponding author. Email: penger@ust.hk

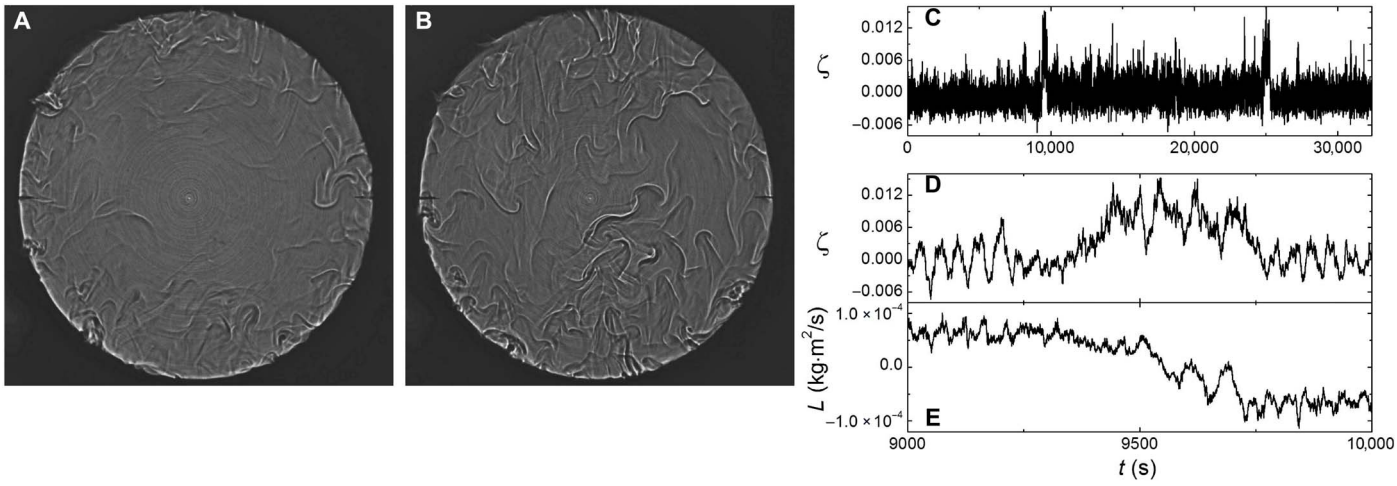

Fig. 1. Characterization of the massive eruption events of thermal plumes. (**A** and **B**) Typical shadowgraph images $I(x, y, t)$ of the convecting fluid at (A) the long steady state and (B) short eruption state. (**C**) Time series of the measured $\zeta(t)$ over a 9-hour-long period of time t. (**D**) Expanded view of $\zeta(t)$ during a massive eruption event of thermal plumes. (**E**) Corresponding time series of the measured angular momentum $L(t)$ of the LSC. All the measurements are made in water ($Pr = 4.4$) with $Ra = 6.2 \times 10^9$.

small temperature variations ($\lesssim$25 K), $n(x, y, t)$ is linearly proportional to $T(x, y, t)$ and one has (*28*, *29*)

$$\zeta(x, y, t) = z_1\gamma\int_0^W \nabla_{||}^2 T(x, y, z, t)dz \quad (1)$$

where $\zeta(x, y, t)\equiv[I_0(x, y) - I(x, y, t)]/I(x, y, t)$ is the normalized inverse intensity with I_0 being the background intensity, z_1 is the distance between the fluid sample and imaging screen, $\gamma = dn/dT$, and $\nabla_{||}^2 = \partial_x^2 + \partial_y^2$. For a thin disc cell, the thermal plumes do not overlap much along the optical path W, and after an average over the cross-sectional area of the cell, Eq. 1 becomes

$$\zeta(t) = \frac{4Wz_1\gamma}{3\kappa D}\delta J(t) = \frac{4Wz_1\gamma}{3\kappa DS_1}\int_{S_1}(J_b - J_t)dS \quad (2)$$

where κ is the thermal conductivity of the fluid, J_b is the heat flux flowing into the system from the bottom conducting plate of area $S_1 = (\pi D/3)W$, and J_t is the heat flux going out of the system from the top conducting plate. Equation 2 thus provides a sensitive null test on whether $\delta J(t)\equiv\langle J_b - J_t\rangle_S$ is balanced or not at any given time. Other details about the experiment are given in Materials and Methods.

Figure 1C shows the time series of the measured $\zeta(t)$ over a 9-hour-long period. There are a few big spikes in the measured $\zeta(t)$ at such times as $t_1 \simeq 9000$ s and $t_2 \simeq 25{,}000$ s. By carefully examining the shadowgraph images and movies (see, e.g., movie S1), we find that these spikes are associated with massive eruptions of thermal plumes across the entire cell, which give rise to large fluctuations of the measured $I(x, y, t)$. These eruption events are rare events and last for 1 to 5 min each time. Depending on the working fluids used, they typically occur 5 to 30 times over a period of 16 hours at $Ra \sim 10^9$. Figure 1D shows an expanded view of $\zeta(t)$ during an eruption event.

The time sequence data reveal that the convective flow in the thin disc has two distinct states: a long steady state (quiet period) interrupted by a short eruption state (active period), which occurs intermittently. Figure 1 (A and B) shows a comparison of the measured shadowgraph images $I(x, y, t)$ at (Fig. 1A) the long steady state and (Fig. 1B) the short eruption state. During the long steady state, there is a stable LSC across the entire cell, with the warm rising plumes on one side and cold falling plumes on the other side of the cell. The measured $\zeta(t)$ oscillates quite regularly in small amplitude, as shown in Fig. 1C. These coherent oscillations are caused by periodic emission of thermal plumes, which has been studied in a previous experiment (*27*).

During the short eruption state, a large amount of thermal plumes simultaneously erupt from the boundary layers, which disrupt the LSC. The plumes are found everywhere in the circular cross section of the cell, and the flow becomes chaotic and disorganized. As the measured $\zeta(t)$ is positive [and hence $\delta J(t)$ is negative, because $\gamma < 0$], the convecting fluid releases a large amount of heat during the eruption. After the eruption, the LSC restarts with an equal probability to rotate in either the same or opposite direction as that of the original LSC. Figure 1E shows the evolution of the angular momentum $L(t)$ of the large-scale flow during the eruption event. The value of L is obtained by tracking the rotational speed of the thermal plumes in the shadowgraph movie using the particle image velocimetry software PIVlab (*30*). During the eruption, L changes from a positive value to a value close to zero and then goes to a negative value of the same amplitude. Figure 1D thus records a reversal event of the LSC.

We now discuss the statistical properties of the measured ζ. Figure 2A shows the normalized histogram $H(\zeta)/H_0$ of the measured ζ from the entire 16-hour-long dataset (black squares) and from the conditionally sampled data with the eruption states removed from the statistics (red circles). The difference between the two curves reveals the effect of the large-amplitude eruption events. A similar effect is also observed in the aqueous solutions of glycerin. Figure 2B shows an example of the measured $H(\zeta)/H_0$ in the 10% glycerin solution ($Pr = 5.7$), with $Ra = 4.1 \times 10^9$. An important feature shown in Fig. 2A (and in Fig. 2B) is that the red curve has a small negative most probable value $\zeta_p = -(8 \pm 2) \times 10^{-4}$, which corresponds to a most probable heat accumulation $(\delta J)_p = 3\kappa D\zeta_p/(4Wz_1\gamma)$ (see Eq. 12 in Materials and Methods). Figure 2C shows the normalized ratio $(\delta J)_p/J_0$ of the most probable heat accumulation $(\delta J)_p$ to the mean heat flux J_0 passing through the convecting fluid as a function of Ra for different working fluids. It is seen that the obtained values of $(\delta J)_p/J_0$ do not change much with Ra for a given fluid but increase slightly with the glycerin concentration. This small amount

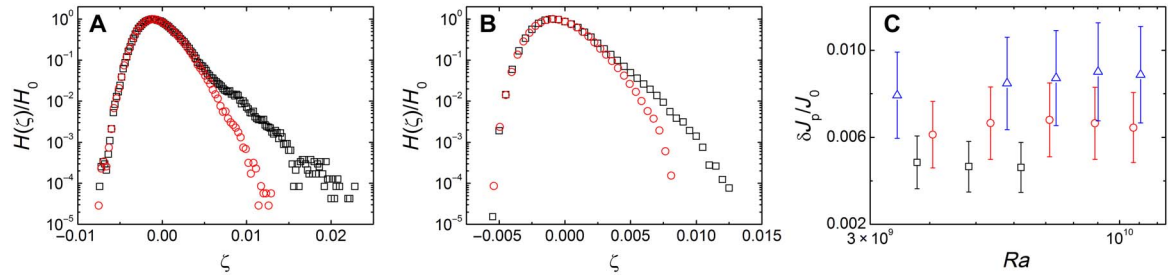

Fig. 2. Statistical properties of the massive eruption events of thermal plumes. (**A**) Normalized histogram $H(\zeta)/H_0$ of the measured ζ in water (Pr = 4.4) with Ra = 6.2×10^9. The black squares are obtained from the whole time series containing both the long steady state and short eruption state. The red circles are obtained when only the dataset in the long steady state is included. (**B**) Measured $H(\zeta)/H_0$ in the 10% glycerin solution (Pr = 5.7) with Ra = 4.1×10^9. The black squares are obtained from the whole time series data, and the red circles are obtained when only the long steady state data are included. (**C**) Normalized most probable heat accumulation $(\delta J)_p/J_0$ as a function of Ra for water (black squares), 10% glycerin solution (red circles), and 20% glycerin solution (blue triangles). The error bars show the experimental uncertainty of the measurements.

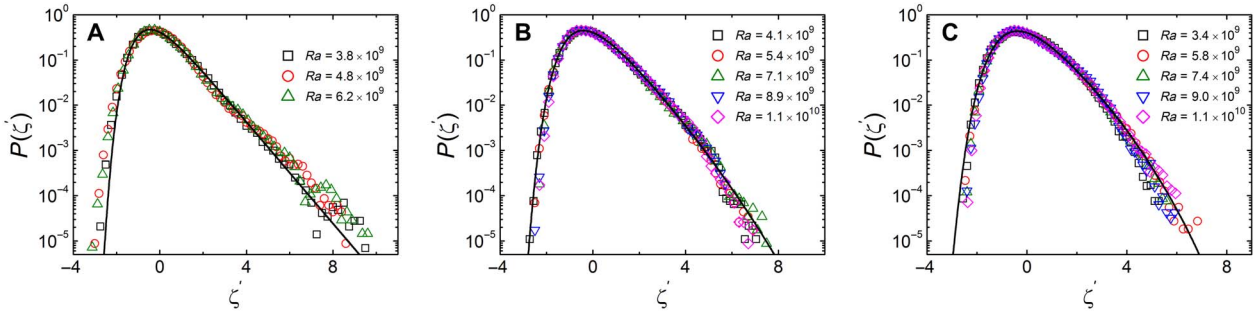

Fig. 3. *Ra* dependence of the PDF of the massive eruption events. (**A** to **C**) Measured PDF $P(\zeta')$ (open symbols) as a function of the normalized variable $\zeta' \equiv \zeta/\sigma_\zeta$ with different values of Ra for (A) water (Pr = 4.4), (B) 10% glycerin solution (Pr = 5.7), and (C) 20% glycerin solution (Pr = 7.6). The solid lines show the fits of the GEV distribution in Eq. 3 to the data points with (A) $\chi = -0.001$, (B) $\chi = -0.04$, and (C) $\chi = -0.07$, respectively.

of heat accumulation (in the range of 0.5 to 0.8%) during the steady state is released in the form of rare massive eruptions of thermal plumes, whose amplitude has a broad distribution. Thus, the net heat flux passing through the convection fluid is balanced only over a long period of time, but not over a relatively short period of time as is commonly believed (*31*).

It is found that the probability density functions (PDFs) $P(\zeta)$ [which are the normalized $H(\zeta)/H_0$] for a given fluid with different values of Ra can all be brought into coincidence once the normalized variable $\zeta' \equiv \zeta/\sigma_\zeta$ is used in the plot. Here, σ_ζ is the SD of ζ. Figure 3A shows the measured $P(\zeta')$ as a function of ζ' for different values of Ra in water. All the measured PDFs $P(\zeta')$ collapse onto a master curve. For water whose refractive index fluctuations are small, we find that the mean value of the measured ζ is $\langle\zeta\rangle \simeq 0$ and that no adjustable parameter is needed to scale the measured $P(\zeta')$. For glycerin solutions at large values of Ra, we find that a small value of $\langle\zeta\rangle$ ($\lesssim \sigma_\zeta$) is needed to scale the measured $P(\zeta')$. In this case, we define $\zeta' = (\zeta - \langle\zeta\rangle)/\sigma_\zeta$. This is caused by relatively large fluctuations of the refractive index in the thermal boundary layers, which introduce experimental uncertainties to the measured ζ. Figure 3 (B and C) shows such scaling plots of the measured $P(\zeta')$ as a function of ζ' for the 10 and 20% glycerin solutions, respectively, at different values of Ra.

The measured PDFs $P(\zeta')$ for the three fluids shown in Fig. 3 can all be well described by the generalized extreme value (GEV) distribution (*32*)

$$P(z) = \frac{1}{\beta}(1+\chi z)^{-(1/\chi+1)} e^{-(1+\chi z)^{-1/\chi}} \quad (3)$$

where the variable $z = (\zeta' - \mu)/\beta$, the scale parameter $\beta = |\chi|/\sqrt{\Gamma(1-2\chi) - \Gamma^2(1-\chi)}$, and the location parameter $\mu = |\chi|[1-\Gamma(1-\chi)]/\left[\chi\sqrt{\Gamma(1-2\chi) - \Gamma^2(1-\chi)}\right]$, with $\Gamma(\ldots)$ being the gamma function. Equation 3 is used to model the limit distribution of properly normalized maxima (with a zero mean and unity variance) of a sequence of independent and identically distributed random variables (*32*). The solid lines in Fig. 3 show the fits of Eq. 3 to the data points, with the shape parameter χ as a fitting parameter. The three sets of data are well described by Eq. 3, with $\chi = -0.001$ (water), $\chi = -0.04$ (10% glycerin solution), and $\chi = -0.07$ (20% glycerin solution), respectively. For $\chi < 0$, Eq. 3 is reduced to the reversed Weibull distribution that has an upper bound $\zeta'_c = \mu - \beta/\chi$, beyond which $P(\zeta') = 0$. From the fitted values of χ, we find the corresponding upper bound $\zeta'_c = 780.3$ for water, $\zeta'_c = 20.0$ for the 10% glycerin solution, and $\zeta'_c = 11.7$ for the 20% glycerin solution. For $\chi = 0$, Eq. 3 is reduced to the Gumbel distribution, which has an exponential tail with an infinite upper bound ($\zeta'_c \to \infty$). Evidently, the measured PDFs $P(\zeta')$ for water, as shown in Fig. 3A, are very close to this limit.

Figure 4A shows the normalized histogram $H(\tau)/H_0$ of the measured time interval τ between the adjacent eruption events. To monitor the LSC evolution over a long period of time, we install 12 thermistors on one of the circular end walls of the cell (see Materials and Methods for more details). A total of ~1000 eruption events are recorded for each Ra over a period of 1 month. The measured $H(\tau)/H_0$ is well described by a simple exponential function, $H(\tau)/H_0 \simeq \exp(-\tau/\tau_0)$ (color-coded lines), indicating that the massive eruption events occur randomly

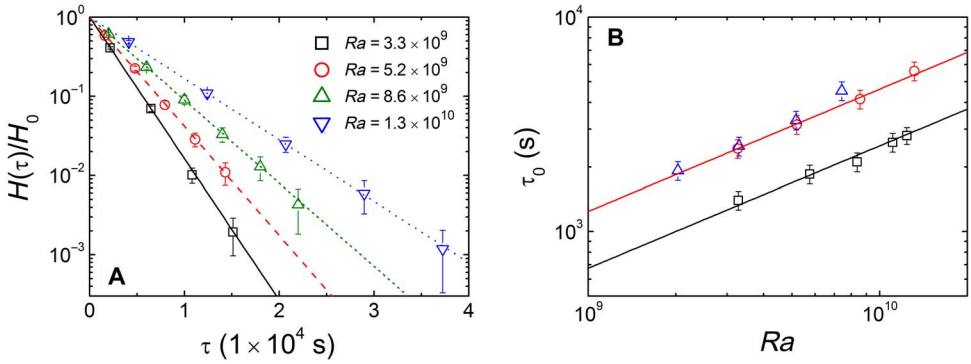

Fig. 4. Statistical properties of the time interval τ between adjacent eruption events. (**A**) Normalized histogram $H(\tau)/H_0$ as a function of τ for the 10% glycerin solution at four different values of *Ra*. The error bars indicate the SD of the measurements. The color-coded lines show the exponential fits, $H(\tau)/H_0 \simeq \exp(-\tau/\tau_0)$, to the data points with τ_0 = 2430 s (black solid line), 3150 s (red dashed line), 4140 s (green short dashed line), and 5600 s (blue dotted line). (**B**) Obtained mean time interval τ_0 between adjacent eruption events as a function of *Ra* for three different fluids: water (blue triangles), 10% glycerin solution (red circles), and 20% glycerin solution (black squares). The error bars show the experimental uncertainty of the measurements. The solid lines (color coded) are the power-law fits, $\tau_0 = aRa^{\beta}$, to the data points, with a = 0.0092 and β = 0.57 ± 0.1 for the red circles and a = 0.005 and β = 0.57 ± 0.1 for the black squares.

and follow the Poisson statistics. Similar exponential distributions were also observed in previous experiments (*15*–*17*).

Figure 4B shows how the obtained mean time interval τ_0 between adjacent eruption events changes with *Ra* for three different working fluids. The measurements for the 10 and 20% glycerin solutions are made at the same bulk temperature 40°C, and their Prandtl numbers are *Pr* = 5.7 and *Pr* = 7.6, respectively. The measurement for water is made at the bulk temperature 27.7°C, and its Prandtl number (*Pr* = 5.7) is the same as that for the 10% glycerin solution. It is seen that the three datasets can all be described by the power law, $\tau_0 = aRa^{\beta}$, with the same exponent β = 0.57 ± 0.1 (solid lines). The power-law amplitude a is found to change with *Pr*. The convecting fluids with a larger value of *Pr* have a smaller value of a.

DISCUSSION

The above measurements reveal that, for the same convecting fluid (same *Pr*), eruption events occur less frequently with increasing *Ra*. At the same *Ra*, the eruption events occur more frequently with increasing values of *Pr* (higher glycerin concentration). It is also found that less frequent eruptions (with a larger value of τ_0) tend to have a larger amplitude. The experiment shows that reversals of the LSC in the thin disc are caused by rare fluctuations in the temperature field with a massive eruption of thermal plumes, which disrupts the existing LSC across the circular disc and resets its rotational direction.

While we are unable to pinpoint the exact cause for the massive eruption of thermal plumes at the moment, we find that the functional form of the measured PDFs $P(\zeta')$ of the eruption amplitude ζ' provides a useful clue to the physical origin of the massive eruption of thermal plumes. As shown in Fig. 3, the measured $P(\zeta')$ follows the GEV distribution with an upper bound ζ_c', which decreases with increasing glycerin concentration (or increasing *Pr*) and consequently reduces the amplitude of typical eruption events. Physically, we believe that the value of ζ_c' is link to the "dynamic heat capacity" of the flow field. For the convective flow in water, its dynamic heat capacity is much larger than that of the glycerin solutions, allowing more heat to be accumulated during the quiet period. As a result, less frequent but larger amplitude eruption events of thermal plumes are observed in this system. For the convective flow in the glycerin solutions, it has a smaller value of the dynamic heat capacity and a relatively larger amount of heat is accumulated in the system (see Fig. 2C). Consequently, more frequent eruption events of smaller amplitude are observed in the glycerin solutions.

It remains unclear how the massive eruption events are triggered in the closed convection cell. In a recent study of reversals of the large-scale velocity and magnetic fields, Gallet *et al.* (*24*) provided an interesting symmetry argument, suggesting that reversals of the large-scale flow can be realized either by spontaneous fluctuations with a large enough amplitude or by an externally imposed symmetry breaking in the boundary conditions. These two effects can introduce an intermediate flow mode of different symmetry (such as a quadrupolar mode), which promotes the reversals. While our experiment has shown that reversals of the LSC in the thin disc cell are caused by the fundamental instabilities in the temperature field rather than in the velocity (or magnetic) field, we believe that the symmetry argument by Gallet *et al.* may also shed light on the instabilities in the temperature field.

At the moment, we can think of two possible mechanisms for the massive eruption of thermal plumes. The first mechanism is that, as the heat is continuously accumulated inside the closed convection cell during the quiet period, the system is driven into a critical state at which the boundary layers become supersensitive to turbulent fluctuations in the system, which trigger the massive eruption of thermal plumes. It is possible that the small heat accumulation in the closed convection cell is caused by some minute symmetry breaking either in the bulk convecting medium (the fluids used in this experiment, however, are homogeneous and isotropic) or in the boundary conditions. For example, the LSC during the quiet period establishes a unique spatial distribution of thermal plumes, with warm plumes accumulated on the rising side of the LSC and cold plumes on the falling side of the LSC. This lateral distribution of thermal plumes, in turn, imposes a small temperature difference between the left-hand side and the right-hand side of the cell wall (see, e.g., fig. S6). Non–Oberbeck-Boussinesq effects of the convecting fluid, on the other hand, make the upper and lower boundary layers to be different in thickness and viscosity (*31*, *33*, *34*).

The second possible mechanism is that the massive eruption of thermal plumes is simply a result of spontaneous fluctuations in turbulent thermal convection. Because of the intrinsic nature of nonlinear interactions, the emission of thermal plumes from the boundary layers in the closed convection cell is chaotic with a small

probability to produce fluctuations of extreme amplitude. The maximum amplitude of these rare extreme fluctuations, however, is bounded from the above because the total heat flux passing through the closed convection cell is kept at a contact value. Further theoretical and numerical investigations are needed to fully understand the nature of these rare but massive eruption events, which can produce such marked effects as the disruption of the entire existing flow field and the development of a new flow pattern across the whole convection cell.

MATERIALS AND METHODS

Convection cell

Details about the convection cell used in this experiment have been described elsewhere (*27*, *35*), and here, we only mention some key points. As shown in fig. S1, the convection cell has a shape of thin vertical disc, with its circular cross section aligned parallel to gravity. The top and bottom one-third of the circular sidewall are made of 8-mm-thick copper. The surface of the copper plates in contact with the convecting fluid was electroplated with a thin layer of nickel. The remaining one-third of the sidewall on both sides are made of transparent 18-mm-thick Plexiglas. The two flat end walls of the cell are also made of the same type of Plexiglas. Two silicon rubber film heaters connected in parallel were sandwiched on the back side of the bottom conducting plate to provide constant and uniform heating. The top copper plate is in contact with a cooling chamber consisting of two water channels. The temperature of the top plate was maintained by a temperature-controlled circulator (NESLAB, RTE740), which circulates cooling water with a temperature stability of 10 mK. The temperature of the top and bottom plates was measured at a rate of 2 Hz by two calibrated thermistors with an accuracy of 5 mK. They were embedded in each plate 1 mm away from the surface of the conducting plate.

In this system, the Rayleigh number is defined as $Ra \equiv \psi g \Delta T D^3/(\nu\kappa)$, where g is the gravitational acceleration, ΔT is the temperature difference across the cell height (diameter) D, and Ψ, ν, and κ are the thermal expansion coefficient, kinematic viscosity, and thermal diffusivity of the convecting fluid, respectively. The Prandtl number is defined as $Pr = \nu/\kappa$, which is fixed for a given fluid. The entire convection cell was placed inside a thermostat box, whose temperature was controlled precisely at (40 ± 0.1)°C, which matches the mean temperature of the bulk convecting fluid. At this temperature, the Prandtl number Pr for the three working fluids used was fixed at 4.4 (water), 5.7 (10 wt % glycerin solution), and 7.6 (20 wt % glycerin solution).

This convection cell has two unique features for the experiment attempted here. First, the cell has a circular cross section without any corner to prevent secondary flows, which may destabilize the LSC (*22*). The LSC in the circular cross section has a fly-wheel–like structure with a mean rotating speed U_0 along a fixed orientation most of the time. Because the flow is confined in a thin circular disc, the LSC in the steady state only has a single mode of its simplest form and no other flow modes can be excited in this quasi–two-dimensional (2D) system. Even with these simplifications, the quasi-2D system still has the key features of turbulent convection, which have been observed in the upright cylinders. In particular, we find that the measured Nusselt number Nu as a function of Ra for water is well described by the power law (see more discussions below)

$$Nu = 0.28 Ra^{0.275} \tag{4}$$

which is consistent with the results obtained in the upright cylinders with a fully developed 3D bulk flow (*6*). Second, the thin circular cell allows us to use the shadowgraph technique to visualize the large-scale convective flow and to precisely measure the net accumulation or loss of heat flux across the entire cell.

Measurement of heat transport

The Nusselt number Nu is defined as

$$Nu = J_0/(k\Delta T/D) \tag{5}$$

where J_0 is the net heat flux passing through the convection cell. In the experiment, the temperature of the conducting plates is determined by the average readings of the two thermistors embedded in each plate. The value of J_0 is given by

$$J_0 = \frac{P_{in} - P_b - P_s}{S} \tag{6}$$

where $S = WD$ is the cross-sectional area of the cell at the middle height, P_{in} is the heating power applied to the bottom plate, and P_b and P_s represent the losses of the heating power through the bottom plate and the sidewalls, respectively. The bottom copper plate and Plexiglas sidewalls were encapsulated by a thermal insulation layer made of polystyrene foam. Two thermistors were placed across the insulation layer in each part to measure the conductive heat losses P_b and P_s.

Figure S2 shows the measured Nusselt number Nu as a function of Ra for water ($Pr = 4.4$) in the thin disc cell. It is seen that the measured $Nu(Ra)$ is well described by the power law given in Eq. 4 (solid line).

Shadowgraph measurement

Figure S3 shows the experimental setup of the shadowgraph measurement. A high-quality white light-emitting diode (LED) (LUXEON S1000, Philips Lightning) equipped with a cooling fan was used as a stable white light source. The LED was powered by a DC power supply (PL303, TTi) with a long-term stability of ±1 mA. The working voltage and current of the LED are 25.50 V and 350 mA, respectively, which correspond to a working power of ~9 W. The while light was guided by an optical fiber to a 1-mm-diameter pinhole, which was positioned at the back focal point of a 250-mm-diameter convex lens so that a wide collimating beam of white light is incident normally to the entire circular section of the convection cell. The shadowgraph image was projected onto a white paper screen at a distance $z_1 = 800$ mm away from the back window of the convection cell. A charge-coupled device (CCD) camera with a spatial resolution of 960 × 960 pixels was used to record movies of the shadowgraph images at a sampling rate of 10 frames per second.

Figure S4A shows the measured background image $I_0(x, y)$ of a static (nonconvecting) fluid (water) when there is no temperature difference applied across the top and bottom conducting plates. While the two flat circular windows of the cell are made of polished Plexiglas plates and no visible scratch is found by the naked eye, one can observe residual circular marks in the shadowgraph resulting from the machine work on the Plexiglas surface. Figure S4B shows a typical shadowgraph image $I(x, y, t)$ of a convecting fluid (water) when a temperature difference $\Delta T = 25.2$°C is applied across the convection cell. The convecting fluid contains many cold and warm thermal plumes, which bend the parallel light rays to regions with higher values of the refractive index n per Huygens's principle and form a pattern with bright and dark strips on the observing screen.

Assuming that each image has N pixels, the 2D average of the normalized intensity $\zeta(x, y, t)$ in Eq. 1 over the cross-sectional area A can be carried out by

$$\zeta(t) = \langle \zeta(x, y, t) \rangle_A = \frac{1}{N} \sum_{i=1}^{N} \frac{(I_0)_i - I_i(t)}{I_i(t)}, \quad (7)$$

where i is the pixel label within the bright field. Because the convection cell is thin and thus the thermal plumes do not overlap very much along the optical path W, the 2D average in Eq. 7 is equivalent to a 3D volume average over the entire convecting fluid. In this case, we have (*28*, *29*)

$$\zeta(t) = W z_1 \gamma \left\langle \nabla_{||}^2 T(x, y, z, t) \right\rangle_V \quad (8)$$

where $\gamma = \mathrm{d}n/\mathrm{d}T$. In the experiment, we recorded movies of the shadowgraph images both with and without a temperature difference ΔT across the cell and used Eq. 7 to obtain the time series data $\zeta(t)$ for three convecting fluids at different Rayleigh numbers. At a fixed value of Ra, each movie lasts for 16 hours and thus contains 5.76×10^5 shadowgraph images in total.

With the special design of the thin disc cell, the volume average $\langle \ldots \rangle_V$ in Eq. 8 can be rewritten as

$$\left\langle \nabla_{||}^2 T \right\rangle_V = -\frac{1}{kV} \int_{S_0} \mathbf{J} \cdot \mathrm{d}\mathbf{S} \quad (9)$$

where $\mathbf{J} = -k\nabla_{||} T$ is the local conductive heat flux across the circular sidewall S_0 of the convection cell. Here, the cell volume is $V = \pi(D/2)^2 W$ and the surface area of each conducting plate is $S_1 = (\pi D/3) W$. With Eqs. 8 and 9, we have

$$\zeta(t) = \frac{4 W z_1 \gamma}{3 \kappa D} \delta J(t) \quad (10)$$

where

$$\delta J(t) = \frac{1}{S_1} \int_{S_1} (J_\mathrm{b} - J_\mathrm{t}) \mathrm{d}S \quad (11)$$

is the net accumulation or loss of heat flux across the entire convecting fluid. Above, J_b is the heat flux flowing into the system from the bottom conducting plate, and J_t is the heat flux going out of the system from the top conducting plate. All other parts of the cell are assumed to be adiabatic, and thus, they do not contribute to $\delta J(t)$. Because γ is a negative number, $\zeta(t)$ and $\delta J(t)$ have opposite signs.

With the measured heat flux J_0, Eq. 10 can be rewritten in a dimensionless form

$$\frac{\delta J}{J_0} = \frac{3 D^2 \zeta}{4 W z_1 \gamma \Delta \mathrm{T} \mathrm{Nu}} \quad (12)$$

Equation 12 thus provides a sensitive null test on whether the net heat flux passing through the convection cell is balanced or not.

Calibration of the shadowgraph measurement

In the experiment, great care was taken to ensure that the assumptions made in the above for the shadowgraph technique are valid for our convection cell. The entire shadowgraph setup was placed inside a thermostatic box, whose temperature is controlled precisely at (40 ± 0.1)°C, which matches the mean temperature of the bulk convecting fluid. At this temperature, the heat exchange between the insulating walls of the convection cell and their surroundings is minimal, and thus, the adiabatic assumption for these insulating walls is valid. The entire box was fully covered by black cloths so that no ambient light can affect the shadowgraph images.

To test the stability of the light source, we used a CCD camera to record a 10-hour movie of the static background $I_0(x, y, t)$, from which we obtain the time series data of the background intensity per image

$$I_0(t) = \sum_{i=1}^{N} (I_0(x, y, t))_i \quad (13)$$

where N is the number of pixels within the bright field in each image. From the calculated mean value $\langle I_0(t) \rangle_t$ and SD σ_0, we find the ratio $\sigma_0 / \langle I_0(t) \rangle_t \lesssim 0.04\%$. This value of background fluctuation is more than 10 times smaller than the measured signals.

An important assumption made in deriving Eq. 8 is that the refraction of the light beam passing through the sample is so small that the paraxial approximation can be applied. This is ensured by use of a thin-layer fluid of thickness $W = 2.0$ mm. As each hot (cold) thermal plume serves as a divergent (convergent) lens, one can estimate its effect as follows. The deflection angle $\varepsilon(x, y)$ of the light beam is given by (*28*)

$$\varepsilon \simeq W |\nabla n(x, y)| \simeq - W \gamma |\nabla T(x, y)| \quad (14)$$

where $\gamma = -1.455 \times 10^{-4} K^{-1}$ for water and the typical value of $|\nabla T|$ for a plume is 0.4 K/mm. With these values, we find $\varepsilon \simeq 10^{-3}$ radian, and the corresponding positional shift on the shadowgraph screen is $\varepsilon z_1 \lesssim$ 0.8 mm. For the CCD camera used in the experiment, its resolution is 0.21 mm/pixel so that this drift is roughly 4 pixels on the final image. This is even smaller than the smallest defects in the system. For example, the smallest dimension of the residual circular marks as shown in fig. S4A is approximately 20 pixels.

Measurement of LSC

To monitor the LSC over a long period of time, we installed 12 thermistors on a circular end wall of the cell. They were embedded in 12 blind holes that are drilled from the outside into the inner surface of the end wall with a distance of 0.5 mm from the fluid surface. As shown in fig. S5, these holes were arranged along a circle of radius 71 mm with an equal azimuthal separation. The thermistors used (Omega 44006) have a diameter of 2.4 mm and a time constant of ~1 s, and they were calibrated individually with an accuracy of 5 mK. A multichannel multimeter was used to measure the resistance value of each thermistor at a sampling rate of 1.3 Hz. The obtained resistance values were then converted to the temperature $T_i(t)$ at each location $i = 1,\ldots, 12$. A similar setup has been used previously for the study of LSC in upright cylinders (*16*).

Figure S6 shows an example of the measured temperature variations as a function of the azimuthal angle θ. The LSC establishes a unique spatial distribution of thermal plumes, with warm plumes accumulated on the rising side of the LSC and cold plumes on the falling side of the LSC. This plume distribution, in turn, imposes a characteristic temperature pattern on the inner surface of the cell's end wall, which was

mapped out by the 12 thermistors. The data points are well described by the function (*16*)

$$T_i(t) = T_0(t) + \delta(t)\cos\left((i-1)\frac{\pi}{6} - \theta_0(t)\right) \quad (15)$$

where T_0 is the bulk fluid temperature and i = 1,..., 12 indicates the angular position of each thermistor, as shown in fig. S6. In Eq. 15, δ is a measure of the amplitude of LSC, and θ_0 ($-\pi \le \theta_0 < \pi$) determines the angular position of the rising (warmer) part of the LSC. For example, if the LSC rotates clockwise as shown in fig. S5, θ_0 will stay in the lower left corner of the circular plate. The solid line in fig. S6 shows a fit of Eq. 15 to the data points, with T_0, δ, and θ_0 as three fitting parameters. The fitted value of T_0 agrees well with the directly measured bulk fluid temperature.

Figure S7 shows the time evolution of the obtained $\theta_0(t)$ for two characteristic eruption events. When an eruption occurs, the LSC is disrupted and so does the large-scale temperature pattern. As a result, θ_0 goes to a value close to zero. After the eruption, LSC restarts and establishes a new temperature pattern so that θ_0 goes back to its steady-state value. The sign of θ_0 can be either the same or opposite to its original sign. The former represents a cessation of LSC (black squares), and the latter represents a reversal of LSC (red circles). In the experiment, we define a new eruption taking place when the absolute value of $\theta_0(t)$ becomes smaller than a critical value, $|\theta_0(t)| \le \theta_c$ = 0.005. In practice, we find that the number of the eruption events counted does not change much with the chosen value of θ_c. For example, the difference in the eruption events counted between θ_c = 0.005 and θ_c = 0.05 is less than 5%. With this definition, we find the starting time of each eruption event and the time interval τ between the adjacent eruption events.

SUPPLEMENTARY MATERIALS

Supplementary material for this article is available at http://advances.sciencemag.org/cgi/content/full/4/11/eaat7480/DC1

Fig. S1. End view of the actual convection cell used in the experiment.
Fig. S2. Measured Nusselt number *Nu* as a function of *Ra* for water in the thin disc cell.
Fig. S3. Experimental setup of the shadowgraphic measurement.
Fig. S4. Background and typical turbulent shadowgraphic images.
Fig. S5. Arrangement of the 12 thermistors on the circular end wall for the measurement of LSC.
Fig. S6. An example of temperature variations measured by the 12 thermistors as a function of their azimuthal angle θ.
Fig. S7. Time evolution of the obtained $\theta_0(t)$ for two characteristic eruption events.
Movie S1. Measured shadowgraphic movie showing a reversal event of the large-scale circulation in the thin disc cell.

REFERENCES AND NOTES

1. G. A. Glatzmaier, R. S. Coe, L. Hongre, P. H. Roberts, The role of the Earth's mantle in controlling the frequency of geomagnetic reversals. *Nature* **401**, 885–890 (1999).
2. P. H. Roberts, G. A. Glatzmaier, Geodynamo theory and simulations. *Rev. Mod. Phys.* **72**, 1081–1123 (2000).
3. G. D. Holman, Solar eruptive events. *Phys. Today* **65**, 56 (2012).
4. M. S. Miesch, J. Toomre, Turbulence, magnetism, and shear in stellar interiors. *Annu. Rev. Fluid Mech.* **41**, 317–345 (2009).
5. F. H. Busse, Convection driven zonal flows and vortices in the major planets. *Chaos* **4**, 123–134 (1994).
6. G. Ahlers, S. Grossmann, D. Lohse, Heat transfer and large scale dynamics in turbulent Rayleigh-Bénard convection. *Rev. Mod. Phys.* **81**, 503–537 (2009).
7. G. Ahlers, Trend: Turbulent convection. *Physics* **2**, 74 (2009).
8. R. Krishnamurti, L. N. Howard, Large-scale flow generation in turbulent convection. *Proc. Natl. Acad. Sci. U.S.A.* **78**, 1981–1985 (1981).
9. B. Castaing, G. Gunaratne, F. Heslot, L. Kadanoff, A. Libchaber, S. Thomae, X.-Z. Wu, S. Zaleski, G. Zanetti, Scaling of hard thermal turbulence in Rayleigh-Bénard convection. *J. Fluid Mech.* **204**, 1–30 (1989).
10. Y.-B. Du, P. Tong, Turbulent thermal convection in a cell with ordered rough boundaries. *J. Fluid Mech.* **407**, 57–84 (2000).
11. X.-L. Qiu, P. Tong, Large-scale velocity structures in turbulent thermal convection. *Phys. Rev. E* **64**, 036304 (2001).
12. H.-D. Xi, S. Lam, K.-Q. Xia, From laminar plumes to organized flows: The onset of large-scale circulation in turbulent thermal convection. *J. Fluid Mech.* **503**, 47–56 (2004).
13. C. Sun, K.-Q. Xia, P. Tong, Three-dimensional flow structures and dynamics of turbulent thermal convection in a cylindrical cell. *Phys. Rev. E* **72**, 026302 (2005).
14. S. Cioni, S. Ciliberto, J. Sommeria, Strongly turbulent Rayleigh-Bénard convection in mercury: Comparison with results at moderate Prandtl number. *J. Fluid Mech.* **335**, 111–140 (1997).
15. K. R. Sreenivasan, A. Bershadski, J. J. Niemela, Mean wind and its reversal in thermal convection. *Phys. Rev. E* **65**, 056306 (2002).
16. E. Brown, G. Ahlers, Rotations and cessations of the large-scale circulation in turbulent Rayleigh-Bénard convection. *J. Fluid Mech.* **568**, 351–386 (2006).
17. H.-D. Xi, K.-Q. Xia, Cessations and reversals of the large-scale circulation in turbulent thermal convection. *Phys. Rev. E* **75**, 066307 (2007).
18. R. Benzi, Flow reversal in a simple dynamical model of turbulence. *Phys. Rev. Lett.* **95**, 024502 (2005).
19. F. F. Araujo, S. Grossmann, D. Lohse, Wind reversals in turbulent Rayleigh-Bénard convection. *Phys. Rev. Lett.* **95**, 084502 (2005).
20. E. Brown, G. Ahlers, A model of diffusion in a potential well for the dynamics of the large-scale circulation in turbulent Rayleigh-Bénard convection. *Phys. Fluids* **20**, 075101 (2008).
21. M. Breuer, U. Hansen, Turbulent convection in the zero Reynolds number limit. *Europhys. Lett.* **86**, 24004 (2009).
22. K. Sugiyama, R. Ni, R. J. A. M. Stevens, T. S. Chan, S.-Q. Zhou, H.-D. Xi, C. Sun, S. Grossmann, K.-Q. Xia, D. Lohse, Flow reversals in thermally driven turbulence. *Phys. Rev. Lett.* **105**, 034503 (2010).
23. M. Assaf, L. Angheluta, N. Goldenfeld, Rare fluctuations and large-scale circulation cessations in turbulent convection. *Phys. Rev. Lett.* **107**, 044502 (2011).
24. B. Gallet, J. Herault, C. Laroche, F. Pétrélis, S. Fauve, Reversals of a large-scale field generated over a turbulent background. *Geophys. Astrophys. Fluid Dyn.* **106**, 468–492 (2012).
25. M. Chandra, M. K. Verma, Flow reversals in turbulent convection via vertex reconnections. *Phys. Rev. Lett.* **110**, 114503 (2013).
26. R. Ni, S.-D. Huang, K.-Q. Xia, Reversals of the large-scale circulation in quasi-2D Rayleigh-Bénard convection. *J. Fluid Mech.* **778**, R5 (2015).
27. H. Song, E. Villermaux, P. Tong, Coherent oscillations of turbulent Rayleigh-Bénard convection in a thin vertical disk. *Phys. Rev. Lett.* **106**, 184504 (2011).
28. G. S. Settles, *Schlieren and Shadowgraph Techniques* (Springer, 2001), chap. 6.
29. J. R. de Bruyn, E. Bodenschatz, S. W. Morris, S. P. Trainoff, Y. Hu, D. S. Cannell, G. Ahlers, Apparatus for the study of Rayleigh-Bénard convection in gases under pressure. *Rev. Sci. Instrum.* **67**, 2043–2067 (1996).
30. W. Thielicke, E. J. Stamhuis, PIVlab-Towards user-friendly, affordable and accurate digital particle image velocimetry in MATLAB. *J. Open Res. Softw.* **2**, e30 (2014).
31. G. Ahlers, E. Brown, F. F. Araujo, D. Funfschilling, S. Grossmann, D. Lohse, Non-Oberbeck-Boussinesq effects in strongly turbulent Rayleigh-Bénard convection. *J. Fluid Mech.* **569**, 409–445 (2006).
32. M. R. Leadbetter, G. Lindgren, H. Rootzén, *Extremes and Related Properties of Random Sequences and Processes* (Springer-Verlag, 1983), chap. 14.
33. X.-Z. Wu, A. Libchaber, Non-Boussinesq effects in free thermal convection. *Phys. Rev. A* **43**, 2833–2839 (1991).
34. J. Zhang, S. Childress, A. Libchaber, Non-Boussinesq effect: Thermal convection with broken symmetry. *Phys. Fluids* **9**, 1034–1042 (1997).
35. Y. Wang, X. He, P. Tong, Boundary layer fluctuations and their effects on mean and variance temperature profiles in turbulent Rayleigh-Bénard convection. *Phys. Rev. Fluids* **1**, 082301(R) (2016).

Acknowledgments

Funding: This work was supported by RGC of Hong Kong SAR under grant nos. C6004-14G (to P.T.) and AoE/P-02/12 (to P.T.). P.-Y.L. acknowledges the support by the MoST of ROC under grant no. 104-2112-M-008-003-MY3. H.S. acknowledges the support by the Shenzhen Research Start-up Fund for Advanced Talents under grant no. 827-000112.

Author contributions: Y.W. performed the experiments. H.S. participated in the early experiments. Y.W., P.-Y.L., and P.T. analyzed and interpreted data and wrote the paper. Y.W. and P.T. designed the experiments. P.T. supervised the project. **Competing interests:** The authors declare that they have no competing interests. **Data and materials availability:** All data needed to evaluate the conclusions in the paper are present in the paper and/or the Supplementary Materials. Additional data related to this paper may be requested from the authors.

Submitted 30 March 2018
Accepted 23 October 2018
Published 21 November 2018
10.1126/sciadv.aat7480

Citation: Y. Wang, P.-Y. Lai, H. Song, P. Tong, Mechanism of large-scale flow reversals in turbulent thermal convection. *Sci. Adv.* **4**, eaat7480 (2018).

ScienceAdvances

Mechanism of large-scale flow reversals in turbulent thermal convection

Yin Wang, Pik-Yin Lai, Hao Song and Penger Tong

Sci Adv **4** (11), eaat7480.
DOI: 10.1126/sciadv.aat7480